Lawrence Berkeley National Laboratory
LBL Publications

Title
Elucidating Performance Limitations in Alkaline-Exchange- Membrane Fuel Cells

Permalink
https://escholarship.org/uc/item/6vc351jx

Journal
Journal of The Electrochemical Society, 164(11)

ISSN
0013-4651

Authors
Shiau, Huai-Suen
Zenyuk, Iryna V
Weber, Adam Z

Publication Date
2017

DOI
10.1149/2.0531711jes

Peer reviewed

eScholarship.org Powered by the California Digital Library
University of California

JES Focus Issue on Mathematical Modeling of Electrochemical Systems at Multiple Scales in Honor of John Newman

Elucidating Performance Limitations in Alkaline-Exchange-Membrane Fuel Cells

Huai-Suen Shiau,[a] Iryna V. Zenyuk,[b,*] and Adam Z. Weber[a,*,z]

[a]*Energy Conversion Group, Energy Technology Area, Lawrence Berkeley National Laboratory, Berkeley, California 94720, USA*
[b]*Department of Mechanical Engineering, Tufts University, Medford, Massachusetts 02155, USA*

Water management is a serious concern for alkaline-exchange-membrane fuel cells (AEMFCs) because water is a reactant in the alkaline oxygen-reduction reaction and hydroxide conduction in alkaline-exchange membranes is highly hydration dependent. In this paper, we develop and use a multiphysics, multiphase model to explore water management in AEMFCs. We demonstrate that the low performance is mostly caused by extremely non-uniform distribution of water in the ionomer phase. A sensitivity analysis of design parameters including humidification strategies, membrane properties, and water transport resistance was undertaken to explore possible optimization strategies. Furthermore, the strategy and issues of reducing bicarbonate/carbonate buildup in the membrane-electrode assembly with CO_2 from air is demonstrated based on the model prediction. Overall, mathematical modeling is used to explore trends and strategies to overcome performance bottlenecks and help enable AEMFC commercialization.
© The Author(s) 2017. Published by ECS. This is an open access article distributed under the terms of the Creative Commons Attribution 4.0 License (CC BY, http://creativecommons.org/licenses/by/4.0/), which permits unrestricted reuse of the work in any medium, provided the original work is properly cited. [DOI: 10.1149/2.0531711jes] All rights reserved.

Manuscript submitted April 7, 2017; revised manuscript received June 14, 2017. Published July 15, 2017. *This paper is part of the JES Focus Issue on Mathematical Modeling of Electrochemical Systems at Multiple Scales in Honor of John Newman.*

Among existing fuel-cell types, alkaline-exchange-membrane fuel cells (AEMFCs) or hydroxide-exchange-membrane fuel cells (HEMFCs) have intriguing features as compared to proton-exchange-membrane fuel cells (PEMFCs). Their advantage is mainly the possibility of using non-noble catalysts due to faster oxygen-reduction-reaction (ORR) kinetics in alkaline media than in acidic media[1–4] as well as perhaps the use of less expensive hydrocarbon membranes. Disadvantages of AEMFCs include lower hydrogen-oxidation-reaction (HOR) kinetics, more complicated water management, and lower intrinsic conductivity for hydroxide compared to proton transport.[5–13] In addition, CO_2 in the air reacts with hydroxide ions to form bicarbonate and carbonate ions, possibly hindering the terrestrial development of AEMFCs by removing hydroxide available for HOR and further limiting hydroxide conductivity.[14,15] Compared to conventional alkaline fuel cells (i.e., using a liquid electrolyte of potassium hydroxide), AEMFCs use a polymeric membrane and should have better tolerance for CO_2 because the precipitate K_2CO_3 is absent in the AEMFC due to the lack of mobile cations in the membrane.[16] However, AEMFCs still suffer a decline in performance due to bicarbonate/carbonate formation in the membrane and catalyst layers (CLs) leading to additional ohmic and kinetic losses.[13–15]

In an AEMFC, the following electrochemical reactions occur in the CLs as follows:

$$\text{Anode:}\quad H_2 + 2OH^- \rightarrow 2H_2O + 2e^- \quad U^0 = -0.8\,\text{V vs. SHE} \qquad [1]$$

$$\text{Cathode:}\quad 1/2O_2 + H_2O + 2e^- \rightarrow 2OH^- \quad U^0 = 0.4\,\text{V vs. SHE} \qquad [2]$$

$$\text{Net:}\quad H_2 + 1/2O_2 \rightarrow H_2O \quad U^0 = 1.2\,\text{V} \qquad [3]$$

Hydrogen combines with hydroxide ions to produce water in the anode. Oxygen reacts with water to generate hydroxide ions in the cathode. Along with the transport of ions from cathode to anode, electro-osmosis moves water from cathode to anode. As shown in the reactions, AEMFCs are expected to have more complicated water management. Water production by the HOR and electro-osmosis may cause flooding in the anode. Since water is a stoichiometric reactant at the cathode, dehydration may occur and limit ORR kinetics as well as ionic conduction in the membrane and cathode CL, especially at high reaction rates. The effects have to be managed with respect to the typical water-management aspects in the CL to provide sufficient water without causing flooding and limiting oxygen to the reaction site.

Figure 1 shows the schematic of the computational domain for a straight-channel single cell in this study. The domain consists of the membrane and two electrodes comprised of the bipolar plate, land/channel flowfield, gas-diffusion layer (GDL), microporous layer (MPL), and CL. Because of symmetry along the *y*-direction, a half cell is considered for computational efficiency. Note that differential conditions are assumed without considering down-the-channel effects (i.e., high flow rates) to emphasize the water-management issues.

To improve cell performance, mathematical models of alkaline fuel cells and AEMFCs have been developed, yet these do not fully address the intricacies inherent in AEMFC water management. Kimble proposed a model where they took into account the polarization phenomena in the anode, separator, and cathode regions for alkaline fuel cells.[17] Their model predicted that the diffusional resistance of dissolved oxygen in the alkaline thin film is a major limitation at low potentials. A dynamic electrochemical model of an alkaline fuel-cell stack was developed by Duerr to investigate the effects of the load changes on various fuel-cell parameters, such as electrolyte concentration and inlet gas pressure.[18] Water management in an alkaline fuel cell and AEMFC was investigated by Verhaert[19,20] and Jiao,[21] respectively, indicating that the performance is generally improved with anode and cathode humidification. It was also shown via modeling that slight anode pressurization and thinner membrane generally

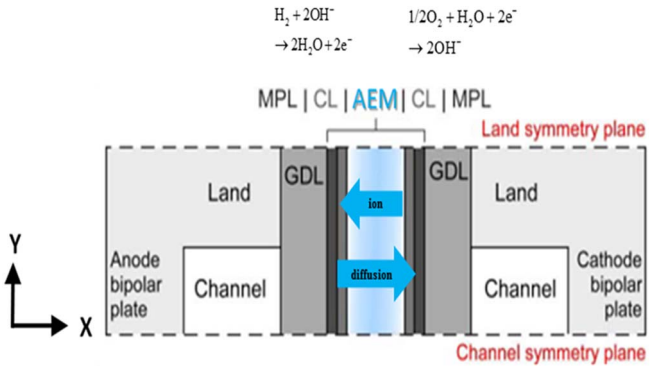

Figure 1. Schematic of AEMFC computational domain.

*Electrochemical Society Member.
zE-mail: azweber@lbl.gov

Downloaded on 2018-02-06 to IP 131.243.172.153 address. Redistribution subject to ECS terms of use (see ecsdl.org/site/terms_use) unless CC License in place (see abstract).

improve the cell performance because the water transport from anode to cathode is enhanced.[22] However, a detailed insight of water management is still lacking in the literature. For example, anode flooding has been investigated by varying the anode inlet relative humidity (RH), pressure, and AEM water permeability. However, cathode drying phenomenon has received much less attention so far. Cathode drying is not only a critical water management issue for performance, but also a possible reason for poor durability of cathode ionomers. It is not clear yet what is the root cause for such a performance-limiting mechanism both experimentally and theoretically, which is the focus of this current study.

In this paper, we develop a two-dimensional model to gain further insight into water/ion/gas transport across multiple layers in a single cell. Special attention is given to the impact of water consumption/production in the CLs on the performance. Asymmetric humidification is used as a diagnostic approach to uncover the dominant water-transport pathway for AEMFCs with different transport properties. The spatial distribution of key components combined with overall performance are shown and discussed for their implication in AEMFC performance limitations. Furthermore, to investigate the impact of CO_2 contamination from ambient air, we incorporate CO_2 reaction kinetics and bicarbonate transport physics into the existing AEMFC model. The strategy of reducing bicarbonate buildup in the membrane-electrode assembly will be demonstrated based on the model prediction. It should be noted that the model was validated as shown in the SI with experimental data,[23] although the qualitative trends are just as important as quantitative comparisons. It should be noted that recent AEMFC performance exceeds that used for validation, but these works typically do not disclose or contain required property data for modeling. Furthermore, the water-management trends identified in this paper would only be exacerbated by higher current-density operation. For example, Mustain and coworkers have recently demonstrated very high power densities after water management aspects were considered in terms of humidification and minimizing dryout and flooding of both the cathode and anode.[24]

Mathematical Model

Membrane and ionomer phase in CLs.—The transport of hydroxide ions and water in the membrane and the ionomer phase in the CLs is described by

$$\sum_{\alpha=l,v} \nabla\cdot\left(\kappa_\alpha\nabla\Phi_2+\frac{\kappa_\alpha\xi_\alpha}{F}\nabla\mu_0\right)=j_{rxn} \quad [4]$$

$$\sum_{\alpha=l,v} \nabla\cdot\left(\frac{\kappa_\alpha\xi_\alpha M_w}{F}\nabla\Phi_2+M_w\left(\alpha_{M_w}+\frac{\kappa_\alpha{\xi_\alpha}^2}{F^2}\right)\nabla\mu_0\right)=R_{v,M} \quad [5]$$

respectively, as derived from concentrated solution theory,[25] where κ_α is the ionic conductivity of the phase α, ξ_α is the electro-osmotic coefficient of the phase α, Φ_2 is the ionic potential and μ_0 is the membrane water chemical potential. Ion transport is driven by the ionic potential gradient and the streaming current. Membrane water transport is governed by electro-osmosis and diffusion. Because there are also two transport modes in the AEM, the ion conductivity and water diffusion coefficient each have vapor- and liquid-equilibrated formulations,[26] which are functions of membrane water content and temperature. The equilibrium membrane water content is thermodynamically related to the vapor-phase water activity and temperature.

Table I. Expressions related to membrane properties and model.

Property	Value	Source
Vapor-equilibrated conductivity, κ_V	$\kappa_V=\begin{pmatrix}0.1334-3.882\times10^{-4}T+(0.01148T-3.909)a_0-\\-(0.06690T-23.01)a_0^2+(0.1227T-42.61)a_0^3-\\-(0.06021T-21.80)a_0^4\end{pmatrix}20\varepsilon_M^{1.5}$	21,34
Liquid-equilibrated conductivity, κ_L	$\kappa_L=5\exp\left[\frac{15{,}000}{R}\left(\frac{1}{T_t}-\frac{1}{T}\right)\right]\varepsilon_M^{1.5}$	25,34
Vapor-equilibrated water content, λ_V	$\lambda_V=\begin{bmatrix}(-0.6a_0^3+0.85a_0^2-0.2a_0+0.153)\times(T-313)\\+39a_0^3-47.7a_0^2+23.4a_0+0.117\end{bmatrix}$	9
Liquid-equilibrated water content, λ_L	$\lambda_L=19$ (for T = 60°C)	26
Total water content, λ	$\lambda=\lambda_V+S(\lambda_L-\lambda_V)$	25
Vapor-equilibrated transport coefficient, α_V	$\alpha_V=\frac{\left(\frac{\lambda_V}{\bar{V}_W\lambda_V+\bar{V}_M}\right)D_V}{RT\left(1-\frac{\lambda_V}{\lambda_V+1}\right)}\varepsilon_M^{1.5}$	25
Vapor-equilibrated diffusion coefficient, D_V	$D_V=D_V^{ref}\left(\frac{\lambda_V\bar{V}_W}{\bar{V}_W\lambda_V+\bar{V}_M}\right)\exp\left(\frac{20000}{R}\left(\frac{1}{T_t}-\frac{1}{T}\right)\right)$ $D_V^{ref}=4x10^{-7}cm^2/s$	25,34
Liquid-equilibrated transport coefficient, α_L	$\alpha_L=\frac{\left(\frac{\lambda_L}{\bar{V}_W\lambda_L+\bar{V}_M}\right)D_L}{RT\left(1-\frac{\lambda_L}{\lambda_L+1}\right)}\varepsilon_M^{1.5}$	25
Liquid-equilibrated diffusion coefficient, D_L	$D_L=D_L^{ref}\left(\frac{\lambda_L\bar{V}_W}{\bar{V}_W\lambda_L+\bar{V}_M}\right)\exp\left(\frac{20000}{R}\left(\frac{1}{T_t}-\frac{1}{T}\right)\right)$ $D_L^{ref}=8x10^{-7}cm^2/s$	25,34
Vapor-equilibrated electro-osmotic coefficient, ξ_V	$\xi_V=(0.183\lambda_V+1.3)\varepsilon_M^{1.5}$	9
Liquid-equilibrated electro-osmotic coefficient, ξ_L	$\xi_L=2.55\exp\left[\frac{4000}{R}\left(\frac{1}{T_t}-\frac{1}{T}\right)\right]\varepsilon_M^{1.5}$	9,25
Interfacial transport coefficient, $k_{v,M}$	$k_{v,M}=10\exp(4.48a_0)$	35
Liquid pressure in the membrane/ionomer, $P_{L,M}$	$P_{L,M}=P_t+\frac{\mu_0}{\bar{V}_L}-\frac{\Delta H_{V-L}}{\bar{V}_L}\left(1-\frac{T}{T_t}\right)-\frac{\Delta C_{p,V-L}}{\bar{V}_L}\left(T-T_t-T\ln\left(\frac{T}{T_t}\right)\right)$	35
Liquid-equilibrated fraction, S	$S=\frac{1}{2}\left[1-erf\left(\frac{\ln(-2\gamma\cos(90.02)/P_{L,M})-\ln(1.25)}{0.3\sqrt{2}}\right)\right]$	25
Activity of water in ionomer phase, a_0	$a_0=\exp\left[\begin{pmatrix}\mu_0-\Delta H_{V-L}(1-\frac{T}{T_t})-\Delta C_{p,V-L}(T-T_t-T\ln(\frac{T}{T_t}))\\-\bar{V}_0(P_{L,M}-P_t)\end{pmatrix}/RT\right]$	35
Chemical potential of water in vapor phase	$\mu_V=H_VM_V\left(1-\frac{T}{T_t}\right)+C_{p,V}M_V\left(T-T_t-T\ln\left(\frac{T}{T_t}\right)\right)+RT\ln\left(\frac{P_V}{P_t}\right)$	35
Chemical potential of water in liquid phase	$\mu_L=H_LM_w\left(1-\frac{T}{T_t}\right)+C_{p,V}M_w\left(T-T_t-T\ln\left(\frac{T}{T_t}\right)\right)+V_w(P_L-P_t)$	35

Downloaded on 2018-02-06 to IP 131.243.172.153 address. Redistribution subject to ECS terms of use (see ecsdl.org/site/terms_use) unless CC License in place (see abstract).

Table II. Physical and material properties taken from literature (noted), or for standard PEMFC and AEMFC components (*),[13,37] operating conditions (#), or assumed (+).

Parameter	Symbol	Value
Standard thermodynamically reversible potential*	$U_0^{\square}$	1.23 V
Inlet temperature#	T_0	60°C
Membrane thickness*		30 μm
CL thickness*		10 μm
MPL thickness*		45 μm
GDL thickness*		190 μm
Land to channel height ratio+		0.11
Specific interfacial area*	a_{Pt}	10^5 cm^{-1}
HOR exchange current density[30,31]	$i_{0,-}^{ref}$	10^{-5} A/cm^2
ORR exchange current density[29,30]	$i_{0,+}^{ref}$	10^{-7} A/cm^2
Reference pressure#	p_{ref}	1 atm
HOR anodic transfer coefficient#	$\alpha_{-,a}$	0.5
HOR cathodic transfer coefficient#	$\alpha_{-,c}$	0.5
ORR anodic transfer coefficient#	$\alpha_{+,a}$	0.5
ORR anodic transfer coefficient#	$\alpha_{+,c}$	0.5
Ionomer volume fraction in CLs+	ε_M	0.12
Porosity in MPLs, and GDLs*		0.3, 0.8
Porosity in cCL*		0.4
Porosity in aCL+		0.6
Solid conductivity*		2.2 S/cm
Total fixed charge concentration*	C_t	3.5 M
Saturated permeability in CLs, MPLs, and GDLs*		6×10^{-17} m^2, 10^{-15} m^2, 10^{-11} m^2
Forward rate constant of Eq. 9[32]	k_1	2.23 m^3/mol/s
Backward rate constant of Eq. 9[32]	k_{-1}	9.71×10^{-5} 1/s
Forward rate constant of Eq. 10[32]	k_2	6×10^6 m^3/mol/s
Backward rate constant of Eq. 10[32]	k_{-2}	5.5 m^3/mol/s
Vapor/liquid rate constant[33]	$k_{L,V}$	10^{-3} cm/s

The expressions for membrane properties are included in Table I.[c] It should be noted that the vapor-equilibrated conductivity is adjusted to be 20 times higher than reported in the references[21,34] to mimic the up-to-date AEM conductivity (see Figure S3).

Gas and liquid transport in the porous media.—Both gas and liquid phases exist in the pores of the various porous media. The gases are treated as ideal, and the Stefan-Maxwell multicomponent transport equations govern the gas transport in the pores. Darcy's law is used to describe the pressure drop of the liquid and gas phases in the porous media. The liquid saturation is associated with the capillary pressure, which is determined from an experimental water–retention curve for hydrophilic CLs (see SI). Within CLs, water exists in three phases: (1) absorbed water in the ionomer, (2) water vapor in the pores, and (3) liquid water in the pores. The transport of water between these three phases is modeled using the difference in chemical potentials,

$$R_{k,l} = k_{k,l}\,(\mu_k - \mu_l) \qquad [6]$$

where $k_{k,l}$ is the kinetic rate constant between phases k and l (see Table II and Table I). This approach accounts for an interfacial resistance for water going to vapor from the liquid or membrane phases but not one for liquid to membrane, consistent with recent experimental findings.[27,28]

Electrochemical reactions.—The reaction rates in the anode and cathode CLs can be calculated using a Tafel equation,

$$i_- = a_{Pt} i_{0,-}^{ref} \left(\frac{p_{H_2}}{p_{ref}}\right)^{0.5} y_{OH^-} \exp\left(\frac{2\alpha_{-,a}F}{RT}\eta_-\right), \quad \eta_- = \Phi_1 - \Phi_2 - U_- \qquad [7]$$

$$i_+ = a_{Pt} i_{0,+}^{ref} \frac{p_{O_2}}{p_{ref}} a_{vapor} \exp\left(\frac{-2\alpha_{+,c}F}{RT}\eta_+\right), \quad \eta_+ = \Phi_1 - \Phi_2 - U_+ \qquad [8]$$

where a_{Pt} is the specific interfacial area, $i_{0,-}^{ref}$ and $i_{0,+}^{ref}$ are the reference HOR and ORR exchange current densities, respectively, p_{ref} is the reference pressure, p_{H_2} and p_{O_2} are the partial pressure of H_2 and O_2, respectively, y_{OH} is the mole fraction of OH^- ion (the total cation concentration is constant), $\alpha_{-,a}$ is the HOR anodic transfer coefficient, $\alpha_{+,c}$ is the ORR cathodic transfer coefficient, η_- and η_+ are the HOR and ORR kinetic overpotentials, respectively, and U_- and U_+ are the HOR and ORR equilibrium potentials, respectively and 1 and 2 refer to the solid and electrolyte phases, respectively. It should be noted that due to the low exchange current densities (see Table II), assuming Tafel kinetics is probably sufficient. The only issue will be in the prediction of very low current densities, which is not the focus of this paper. This is also a difference between PEMFC and AEMFC in that the HOR is typically much more sluggish, especially on Pt as assumed here. Also, unlike in PEMFC, water vapor is a reactant in the ORR, so the water activity in vapor phase is explicitly included. Finally, the term y_{OH^-} is used so that when bicarbonate or carbonate exists its impact on the HOR rate is accounted for (i.e., without CO_2 in the inlet $y_{OH^-} = 1$).

CO_2 reaction kinetics & bicarbonate/carbonate transport.—Two reversible reactions take place when CO_2 is absorbed into the alkaline ionomer phase:

$$CO_2 + OH^- \rightleftharpoons HCO_3^- \qquad [9]$$

where the forward and backward rate constants are k_1 and k_{-1}, respectively (see Table II), and

$$HCO_3^- + OH^- \rightleftharpoons CO_3^{2-} + H_2O \qquad [10]$$

where the forward and backward rate constants are k_2 and k_{-2}, respectively (see Table II).

The transport of hydroxide, bicarbonate, and carbonate ions is described by Eq. 4 with an additional diffusion driving force based on the ion concentration gradient. The ion flux is described by

$$N_i = \kappa_i \nabla\Phi_2 - \frac{\kappa_i \xi_i}{F}\nabla\mu_0 - F D_i \nabla y_i \qquad [11]$$

where i is the ionic species, y_i is the mole fraction of the ion i, and κ_i is the conductivity of the ion i,

$$\kappa_i = z_i F C_t y_i \mu_i \qquad [12]$$

where z_i is the charge of the ion i, C_t is the total fixed charge concentration, and μ_i is the ion mobility. The water absorption isotherm of the alkaline ionomer is assumed to be same in the OH^- form and HCO_3^{-2}/CO_3^- form due to lack of experimental data. An electroneutrality condition is applied to the CL ionomer and membrane

$$y_{HCO_3^-} + 2y_{CO_3^{-2}} + y_{OH^-} = 1 \qquad [13]$$

It should be noted that changes of AEM transport properties (e.g., water diffusivity) due to carbon dioxide interactions with the polymer are not considered.

Numerical methods and boundary conditions.—To solve simultaneously the equations presented above, the commercial finite element software COMSOL Multiphysics 4.4 (COMSOL, Inc., Palo Alto, CA) was used with the MUMPS solver. The mesh consisted of 9450 domain quadrilateral elements and 1022 boundary quadrilateral elements, where increased mesh density was introduced within and near CL domains. The overall boundary conditions used in the simulation are given Table III.

Results and Discussion

Mathematical modeling is ideally suited for breaking down and understanding observed phenomena. Figure 2 shows the polarization breakdown for a cell operating at 100% inlet RH with pure oxygen

[c]It should be noted that there is a need in the community for a baseline AEM (similar to Nafion for PEMFCs) to be chosen and characterized. Thus the modeling values are from various sources, but are believed to be representative of most AEMs.

Downloaded on 2018-02-06 to IP 131.243.172.153 address. Redistribution subject to ECS terms of use (see ecsdl.org/site/terms_use) unless CC License in place (see abstract).

Table III. Boundary conditions.

Variable	Boundary condition	Boundary
Liquid pressure	$P_L = P_G$ for $P_L \geq P_G$	Anode CH|GDL
	$-n \cdot N_L = 0$ for $P_L \leq P_G$	Cathode CH|GDL
Gas pressure	$P_G = P_G^{in}$	Anode CH|GDL
		Cathode CH|GDL
Reactant mass fraction, ω_R	$w_R = \frac{y_R^{in} M_R}{\sum_j y_j^{in} M_j}$	Anode CH|GDL
	$y_R^{in} = (1 - y_V^{in}) y_R^{dry}$	Cathode CH|GDL
Water vapor mass fraction, ω_V	$w_v = \frac{y_V^{in} P^{sat}}{P_G^{in}}$	Anode CH|GDL
		Cathode CH|GDL
Nitrogen mass fraction, ω_D	$w_D = \frac{y_D^{in} M_D}{\sum_j y_j^{in} M_j}$	Anode CH|GDL
	$y_D^{in} = 1 - y_R^{in} - y_V^{in}$	Cathode CH|GDL
Temperature	$T = T_0$	Anode outside edge of Plate
		Cathode outside edge of Plate
Electric potential	$\Phi_1 = 0$ (setting reference potential at the alkaline anode)	Anode outside edge of Plate
	$\Phi_1 = \Phi_{cell}$	Cathode outside edge of Plate
Ionic potential	$-n \cdot \nabla \Phi_2 = 0$	MPL|CL
Membrane chemical potential	$-n \cdot \nabla \mu_0 = 0$	MPL|CL

(no CO_2) at 60°C. It should be noted that cathode oxygen mass transfer is not limiting in this simulation since pure hydrated O_2 feed and differential cell conditions are assumed (note also the lower current densities achieved). Regarding the kinetic loss, the ORR is more limiting than the HOR, but, as expected, the HOR is no longer negligible as it is in PEMFCs for the chosen Pt catalyst (it should be noted that some recent studies suggest that HOR on different catalysts in alkaline can approach that of HOR on Pt in acid).[36] Although both the AEM and cCL significantly contribute to the amount of ionic ohmic loss, the membrane ohmic loss increases much faster than the cCL ohmic loss with higher current density near 1 A/cm^2, leading to a steep dropoff in performance. This is due to the high degree of dehydration at the interface of the cathode and membrane at high current density, causing the ionic resistance to increase significantly. This phenomenon causes the membrane ohmic loss to increase nonlinearly with respect to current density. Even if there is some degree of dehydration due to

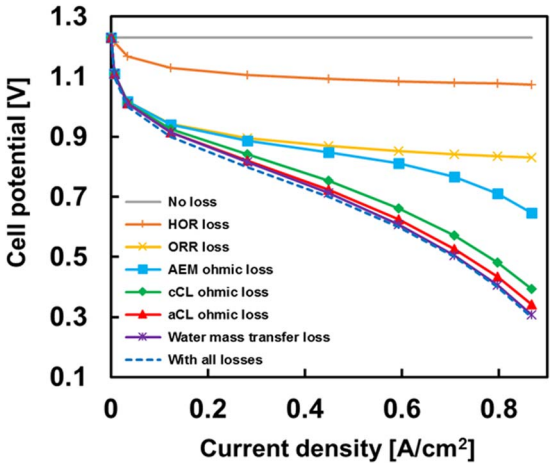

Figure 2. Breakdown of various polarization losses at 100% inlet RH with pure O_2 (no CO_2) and 60°C.

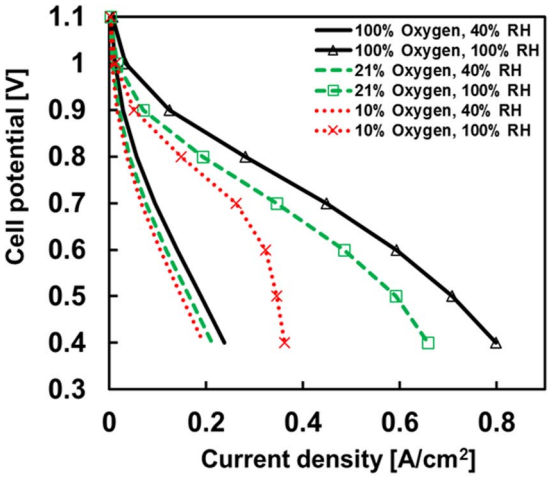

Figure 3. Polarization curves at different inlet RHs at 60°C, 100% dry H_2 feed into the anode and three different dry inlet O_2 mole fractions.

the ORR consuming water, the cathode mass-transfer loss for water vapor is small compared to the ohmic loss because of the high water-vapor diffusivity and since the current density is not high enough. This ohmic loss results in less catalyst being utilized. The strong coupling between OH^- ionic conduction and water transport leads to this increasingly larger ohmic loss (especially for the membrane) that controls the performance, at a current density lower than required to reach significant water mass-transport limitations (within the cathode pores or through the membrane). Finally, the anode hydrogen mass transfer loss is negligible compared to the cathode vapor mass transfer loss, mainly due to the adoption of higher porosity of the anode catalyst layer (aCL).

The local hydration state of the ionomer in the CLs strongly affects the performance because OH^- conductivity is highly dependent on the water content and ORR consumes water as a reactant. Figure 3 shows the influence of external humidification on the polarization curves under differential conditions for three different inlet oxygen mole fractions (1, 0.21, and 0.1). The performance at 0.7 V is improved dramatically with increased humidification of inlet gases mainly due to the increase of ionic conductivity (see SI) and reactant water. At potentials lower than 0.6 V, increase in external humidity from 40 to 100% RH does not improve the performance as much because of the membrane and cCL dehydration, as shown in Figure 2.

The decline in performance at low potentials is more significant as the oxygen mole fraction in the cathode feed decreases from 100 to 10%, indicating that oxygen transport becomes more limiting. Due to the low membrane water diffusivity, water generated by HOR at the anode cannot be efficiently transported through the membrane to the cathode; instead, the pores in the anode catalyst layer may be partially occupied with water, especially when the anode porosity is decreased, as discussed below. In addition, water is generated at the anode and thus flooding affecting oxygen transport is minimized compared to PEMFCs, although at the expense of the more drastic impact of cathode dehydration.

To understand the reaction rates and the limiting effect of CL conductivity, the ORR and HOR reaction distributions for 60% RH are plotted in Figures 4a and 4b, respectively, for different cell potentials. As can be seen, the reaction distribution within either CL is very narrow and close to the membrane, which is indicative of strong ohmic limitations.[37,38] This also indicates a poor utilization of ORR catalyst within the cCL, especially near the cMPL, which would mean increases in the cCL thickness or effective catalyst loading will not improve performance. This is somewhat different than in PEMFCs, where at high current density the reaction distribution is closer to the cCL/cMPL interface due to oxygen transport limitations. Of course,

Downloaded on 2018-02-06 to IP 131.243.172.153 address. Redistribution subject to ECS terms of use (see ecsdl.org/site/terms_use) unless CC License in place (see abstract).

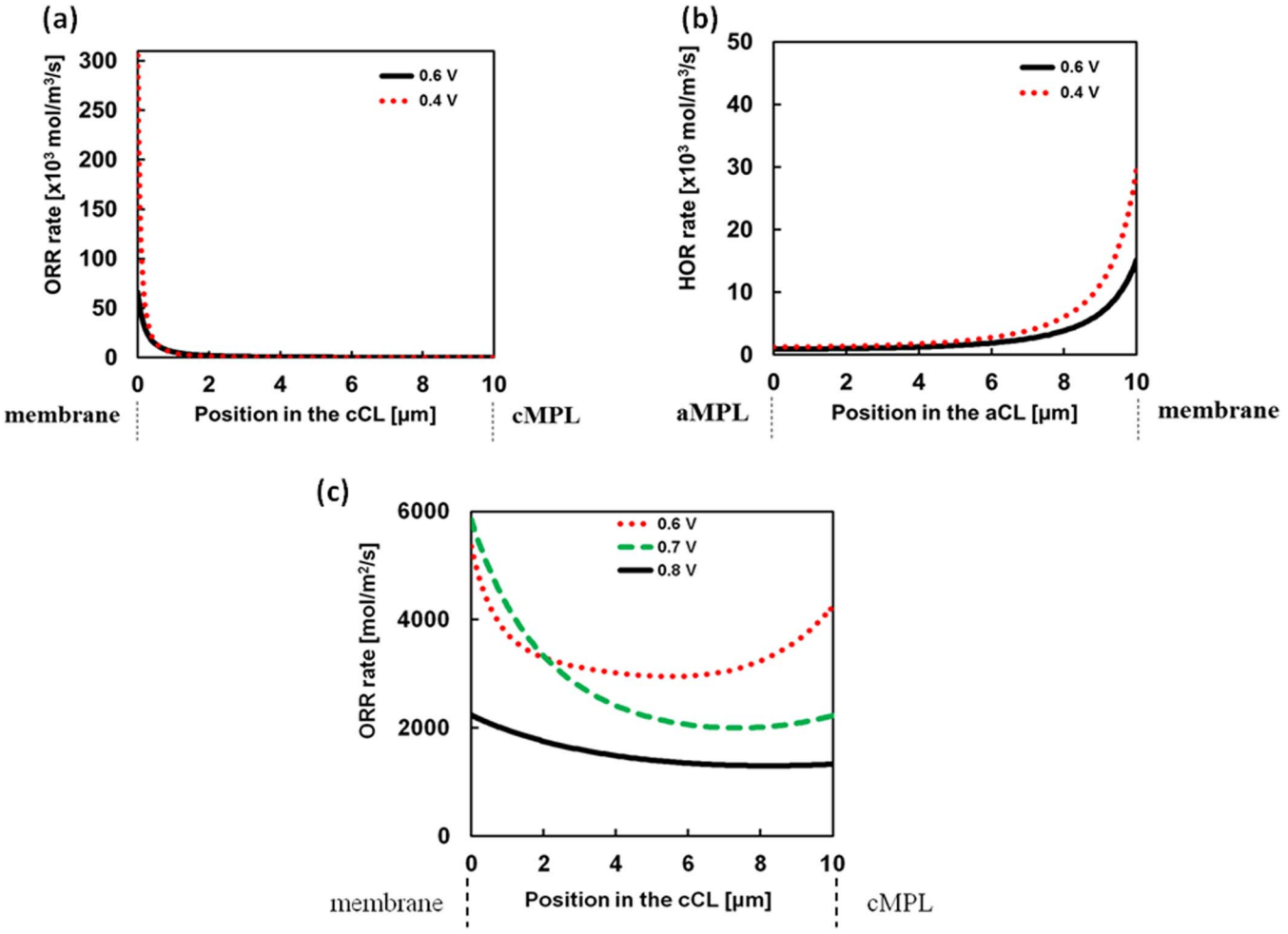

Figure 4. ORR (a) and HOR (b) rate distributions in the respective CLs at 0.6 (solid curve) and 0.4 V (dotted curve) for 60% RH inlet and pure dry oxygen and hydrogen feeds. (c) ORR rate distribution in the cCL at 0.8, 0.7, and 0.6 V for 10% dry O_2 cathode feed with 100% RH.

if oxygen becomes limiting (e.g., near the cell outlet) then a parabolic reaction distribution would occur, which is seen in Figure 4c for low cell potentials and the lower O_2 case (10% or half-air). This figure also demonstrates that humidification up to 100% helps but does not alleviate the ohmic limitations, in agreement with Figure 3. Overall, a significant performance improvement can be achieved by either weakening the water-content dependence of OH^- conductivity or smoothing out the water distribution.

When the AEMFC has a low membrane water diffusivity and low anode porosity, it is possible that cathode dehydration and anode flooding can occur simultaneously, with a similar profile as Figure 4c existing for the aCL. Figure 5a shows that at 100% inlet RH,

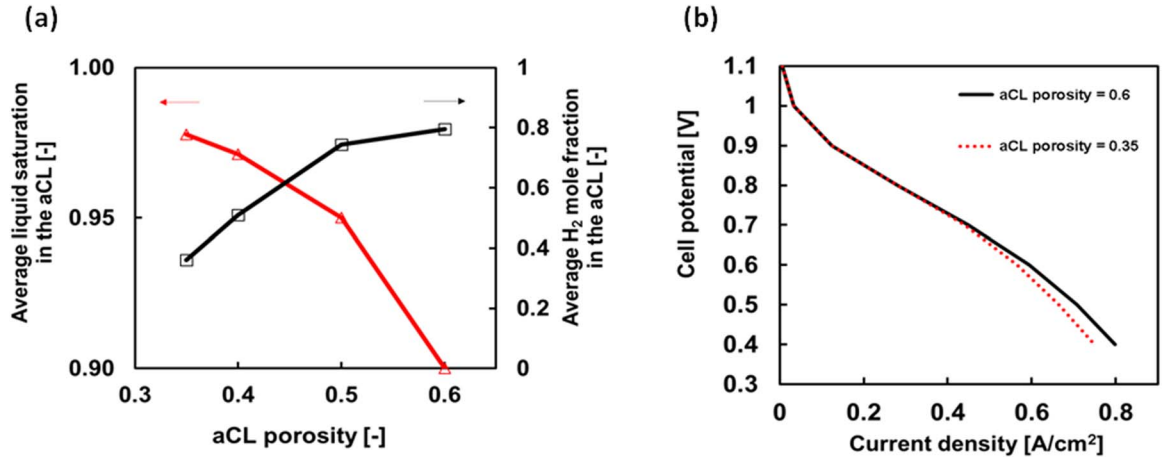

Figure 5. (a) Average liquid saturation and H_2 mole fraction in the aCL as a function of aCL porosity for 100% inlet RH at 0.7 V. (b) Polarization curves at 100% inlet RH for two different aCL porosities.

Downloaded on 2018-02-06 to IP 131.243.172.153 address. Redistribution subject to ECS terms of use (see ecsdl.org/site/terms_use) unless CC License in place (see abstract).

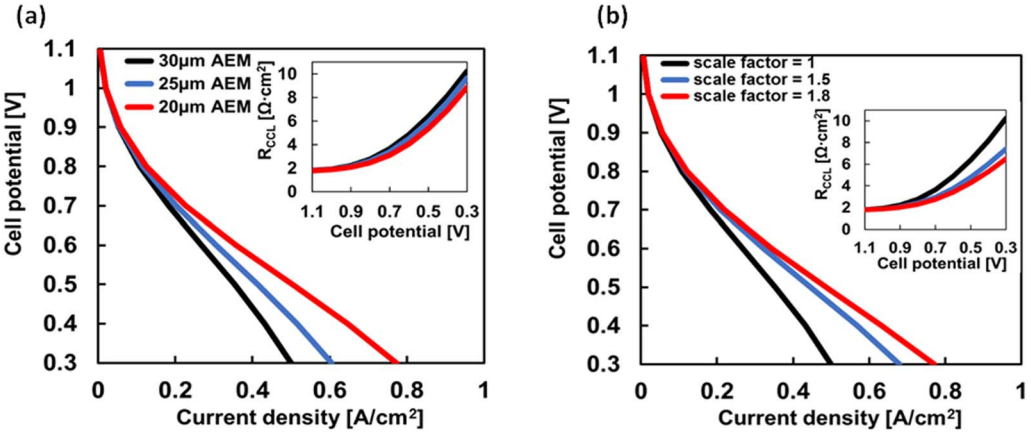

Figure 6. Effect of membrane (a) thickness and (b) water diffusivity on performance with a membrane thickness of 30 μm and a scale factor from the baseline value in Table I. T = 60°C and RH = 60% at both electrode inlets.

when the aCL porosity decreases from 0.6 to 0.35, the average liquid saturation in the aCL increases toward 1 and the average H_2 mole fraction in the aCL significantly decreases due to water generated by HOR and electro-osmosis. Figure 5b shows that the performance at 0.4 V decreases with lower aCL porosity due to increasing anode mass-transfer loss. This tradeoff does not really exist for PEMFC since the anode is effective a water sink and not source.

As Figure 3 and Figure 4 demonstrate, at moderate inlet RH, high current-density operation is limited by low water contents in the cCL ionomer (see baseline curve in Figure 6), which is caused by dehydration in the cathode because of water consumed in the ORR. This dryout results in a dramatic increase in the ionic transport resistance, as seen in Figure 6a inset. To overcome these limitations and facilitate water transport from anode to cathode, a sensitive study was undertaken with respect to the membrane properties. Changing the membrane thickness from 30 to 20 μm reduces the cCL ionic resistance by enhancing water transport from anode to cathode. Although even with a 20 μm membrane, the cCL resistance still increases significantly with lower potentials. Figure 6b shows that higher AEM water diffusivity is more effective in uniformly distributing water between the anode and cathode, as indicated by the inset graph where the cCL ionic resistance increases more slowly over a wide range of potentials for higher AEM water diffusivity. The benefit of maintaining a slowly-changing cCL ionic resistance is that there is no significant drop in performance up to a current density of 1 A/cm^2.

Poor performance under subsaturated humidification is not simply due to mass-transport issues with water, but a consequence of the non-uniform water distribution leading to sluggish OH^- conduction and catalysis in the cCL as well, which are highly water dependent. Although Figure 6 demonstrates that thinner membrane and higher AEM water diffusivity could reduce the potential loss at high current density by enhancing the water back transport through the membrane, the performance limitation at high current density also results from the strong dependence of OH^- conduction on the ionomer water content. At low potentials, the potential loss due to AEM and cCL ohmic limitation is larger than that due to mass-transport issues with water, as seen in Figure 2. The significantly increased cCL ionic resistance (inset in Figure 6) leads to a maximum of ORR rates occurring near the AEM/cCL interface, as show in Figure 4a. Overall, this analysis highly motivates the development of AEMs with enhanced water-transport properties in order to boost the performance of AEMFC to be comparable to PEMFC.

Asymmetric humidification: role of transport resistance.—From above, it is clear that humidity and water balance play a strong role in AEMFC performance. The performance limitation by water deficiency in the cCL can be alleviated by increasing the flux of water to the local cathode reaction sites from the anode inlet (via transport through the membrane) or the cathode inlet (via vapor diffusion through the pores). For operational understanding and optimization, it is important to understand whether the performance is more sensitive to water from the anode or cathode inlet. This should depend on the difference in transport resistances for water entering the cCL from the anode or cathode inlet. The anode inlet RH is more critical to performance if the membrane water-transport resistance is low (high AEM water diffusivity or thin membrane). The cathode inlet RH would be more critical to performance if the membrane water-transport resistance is high (or if the vapor transport resistance in the cathode is low).

To quantify these statements, the effective anode resistance (R_a) against water transport from the anode inlet to the cathode catalyst layer can be described as

$$R_a = R_{aGDL/aMPL} + R_{aCL}^{ionomer} + R_{membrane} \quad [14]$$

The effective cathode resistance (R_c) against water transport from the cathode inlet to the cathode catalyst layer can be described as

$$R_c = R_{cGDL/cMPL} + R_{cCL}^{ionomer} \quad [15]$$

Note that the resistance of vapor absorption into AEM ionomers is not included in calculating the effective resistance here. The expression for the water transport resistance in the ionomer and gas phases can be referenced to the previous work.[35]

The effect of R_a and R_c on polarization curves is demonstrated in Figure 7 under asymmetric humidification of inlet RHs of 80%/10% (either a/c or c/a). There are several ways to vary the difference between R_a and R_c. For example, increasing AEM water diffusivity or decreasing membrane thickness can make $R_a < R_c$, which is related to the above sensitivity analysis of membrane properties. Increasing the effective vapor diffusivity in the cathode (higher porosity or lower tortuosity) can make $R_a > R_c$.

The difference in water transport resistance between anode and cathode is critical to determine the correlation between performance and external humidification. For $R_a > R_c$, the performance with higher cathode RH is better than that with higher anode RH due to the lower water transport resistance from the cathode inlet; the difference in performance becomes significant at high current density. For $R_a < R_c$, the performance with higher anode RH is better than that with higher cathode RH because water transport from the anode inlet has a lower resistance than that from the cathode inlet. By systematically varying the ratio of R_a and R_c, it is found that increasing cathode inlet RH does not necessarily improve performance. In addition, it is seen that the performance variation with asymmetric humidification is more pronounced for $R_a < R_c$ than for $R_a > R_c$, suggesting that performance could be more sensitive to the external humidity when the membrane has a low water transport resistance or when the effective diffusion coefficient of water vapor through the cathode is low. The

Downloaded on 2018-02-06 to IP 131.243.172.153 address. Redistribution subject to ECS terms of use (see ecsdl.org/site/terms_use) unless CC License in place (see abstract).

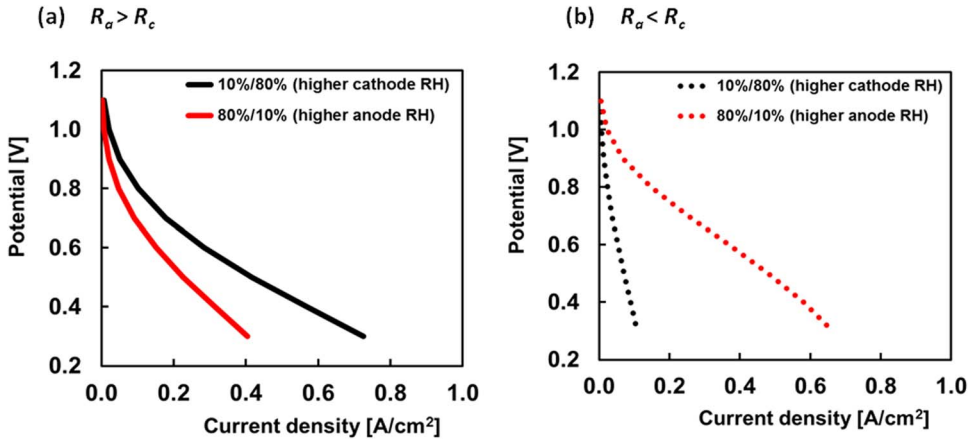

Figure 7. Polarization curves at asymmetric RH (80%/10%) for the case of (a) $R_a > R_c$ and (b) $R_a < R_c$.

above analysis and results are in agreement with Omasta et al., who showed that optimal inlet humidification is critical for achieving high performance as there is a balance between flooding of either electrode and membrane dehydration.[24]

The performance trend in Figure 7 is supported by the spatial distribution of ionomer water content in the AEM and cCL in Figure 8, as well as the magnitude of membrane water flux in Table IV. For $R_a > R_c$, the ionomer water content is higher with higher cathode RH and the magnitude of membrane water flux is higher with higher cathode RH. These two trends substantiate and explain the observation in Figure 7a that performance is enhanced more significantly with increasing cathode RH, compared to increasing anode RH. For $R_a < R_c$, both the water content and the magnitude of the membrane water flux are higher if the anode RH is higher, explaining the result in Figure 7b that performance is enhanced more significantly with increasing anode RH. In addition, the β value, which is the membrane water flux normalized by current density, is consistent with the performance trend in Figure 7. The closer to zero the β value is, the higher the performance, implying that performance can be enhanced by establishing a better balance between membrane water transport and water consumption/generation kinetics. It is interesting to note that β is essentially the same when the anode is less saturated than the cathode for both resistance levels (although the actual water flux and current are different), which demonstrates that the vapor-phase transport and generation at the lower RH dominate the water balance, in agreement with previous studies with PEMFCs.[39,40] However, when the cathode is at lower saturation, this trend ceases to exist namely due to water being a reactant in AEMFCs. Finally, possible existence of interfacial effects and "skin" resistances could be important if they exist in AEMs as they are believed to be in PEMs.[27,41,42]

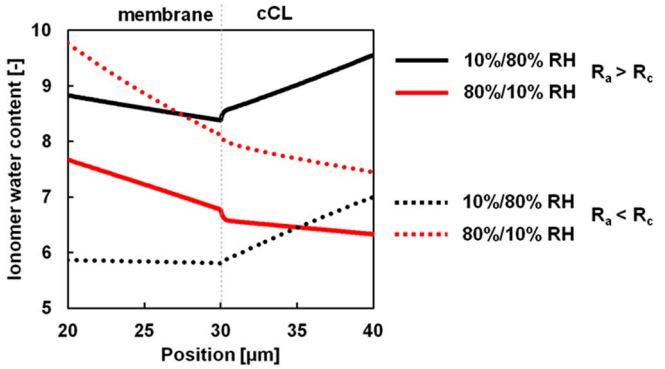

Figure 8. Spatial distribution of ionomer water content in the AEM and cCL at 0.6 V for different asymmetric RHs and dominating resistances.

Impact of carbon dioxide.—Upon exposure to CO_2, even at the concentrations in air, AEMFCs suffer a decline in performance due to assumed bicarbonate formation in the AEM and CLs leading to large ohmic losses.[14,15] To understand the coupling of bicarbonate formation to AEMFC operation, CO_2 reaction kinetics and bicarbonate transport physics are incorporated into the AEMFC model, as detailed above. CO_2 reacts with OH^- to produce HCO_3^- ions, converting the membrane from OH^- form to HCO_3^- form, thereby increasing the membrane ionic resistance.[13,43,44] In addition, this has an exacerbating impact on the HOR kinetic losses due to insufficient reactant OH^- ions (see Eqn. 8). Figure 9a shows the distribution of bicarbonate ion fraction in the anode, membrane and cathode at different cell potentials for a feed concentration of 400 ppm feed CO_2. At high potentials, the rate of OH^- generation (i.e., the ORR rate) is insufficient to remove the (bi)carbonate ions; however, at low potentials, the rate of OH^- generation becomes higher and dominates. Figure 9b shows quantitatively that the bicarbonate content significantly decreases with higher current density and consequently the membrane OH^- conductivity increases. This findings suggests that high current-density operation could restore the membrane from HCO_3^- form to OH^- form, although changes due to AEM properties and reaction kinetics caused by interaction with carbon dioxide and carbonate species may limit the recoverable performance; something under current investigation.

In fact, from the modeling, the performance of AEMFC at 400 ppm CO_2 condition can be comparable to that of CO_2-free AEMFC at high current densities as shown in Figure 9c. At a low current density, the voltage is much lower in the presence of CO_2, but at higher current density, the voltage remains similar between the two conditions, which is attributed to the significantly reduced bicarbonate content. In fact, at true limiting current, the two polarization curves should approach each other. The HCO_3^- ions that are displaced by OH^- ions are purged from the membrane-electrode assembly in the form of CO_2 that appears at the anode outlet. It should be noted that this purging effect is a result of the acid/base reactions (Eqs. 9 and 10) and is driven by the increased hydroxide ion concentration and the need for obeying electroneutrality in the membrane. Although Mustain and coworkers proposed that HCO_3^- and CO_2 might participate in the

Table IV. Current density, membrane water flux and β value at 0.6 V from asymmetric humidification.

RH_{anode} / $RH_{cathode}$	Current density [A/cm²]	Membrane water flux [mol/m²/s]	β [-]
80%/10% RH $R_a > R_c$	0.15	0.059	3.75
10%/80% RH $R_a > R_c$	0.28	−0.069	−2.33
80%/10% RH $R_a < R_c$	0.37	0.027	0.70
10%/80% RH $R_a < R_c$	0.05	−0.013	−2.35

Downloaded on 2018-02-06 to IP 131.243.172.153 address. Redistribution subject to ECS terms of use (see ecsdl.org/site/terms_use) unless CC License in place (see abstract).

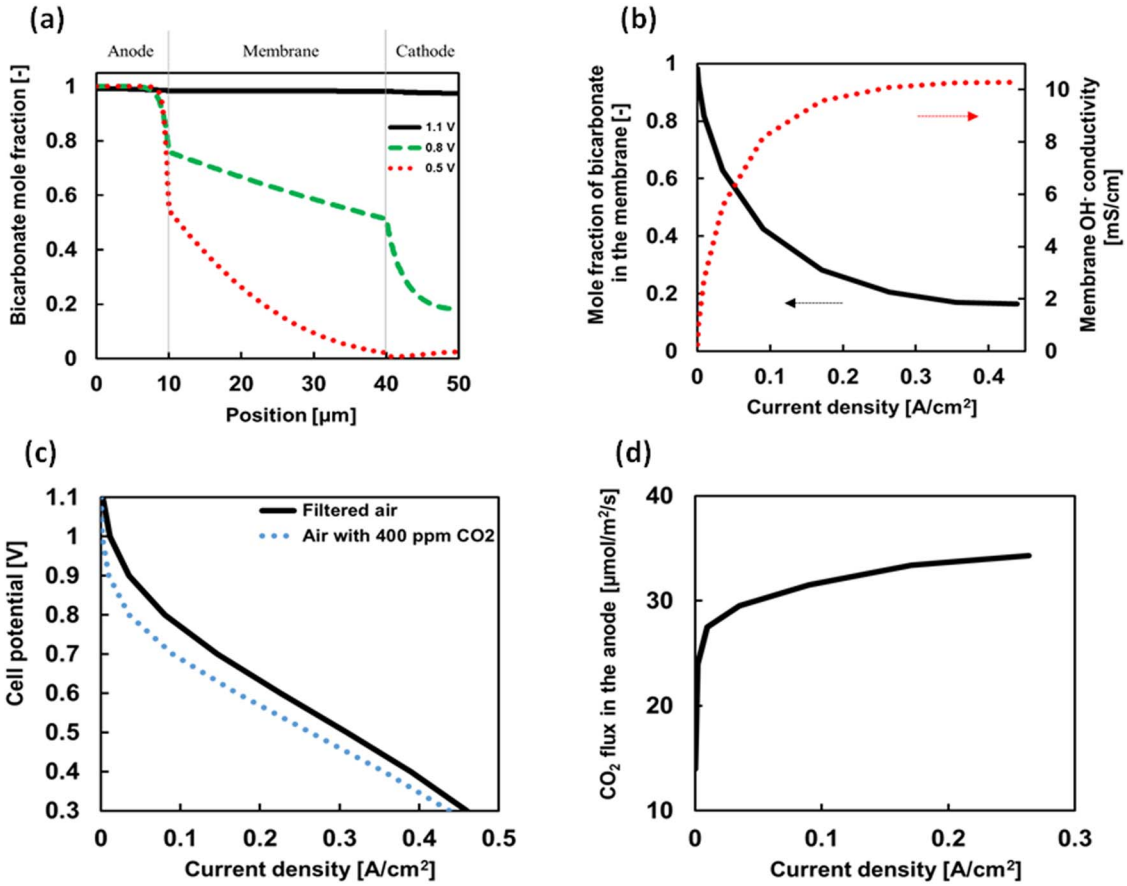

Figure 9. (a) Spatial distribution of the bicarbonate ion fraction in the aCL, AEM, and cCL at different voltages. (b) Bicarbonate ion fraction and membrane OH^- conductivity with current density. (c) Polarization curves with CO_2-free filtered air and air with 400 ppm CO_2. (d) The flux of CO_2 in the anode outlet as a function of current density.

HOR directly, this remains controversial and debatable and is not invoked here explicitly, although it is implicitly considered due to the acid/base reactions, as explained in Table S1. In the mass balance, the source and sink terms for HCO_3^- and CO_2 in the anode and cathode have equal magnitudes but opposite signs. Figure 9d shows that the flux of CO_2 in the anode outlet increases with higher current density, supporting the decrease of HCO_3^- content in the membrane. The model predicts that high current-density operation helps self-purge of CO_2 at the anode in agreement with some experiments,[14,45] leading to performance recovery, although CO_2 buildup at the anode exhaust could be an issue, especially with a recycled H_2 stream or low stoichiometry. Such a buildup will also minimize the effect of the purge due to the equilibrium in the aCL. Furthermore, the model does not account for indirect effects of CO_2 on AEM properties due to plasticization, etc., nor does it account for irreversibilities in the rate constants for the acid/base reactions in AEMs due to inherent interactions and morphological changes between ionic forms, which are currently under investigation. Thus, Figure 9 can be considered a best-case scenario.

Summary

A multiphysics AEMFC model was developed to examine and elucidate steady-state performance bottlenecks and enable strategies to overcome them. At saturated relative humidity, performance is mainly dominated by kinetics at both electrodes and dehydration of the cathode catalyst layer. For low anode porosities, H_2 mass-transport limitations can also become limiting due to anode flooding. At moderate relative humidity, performance is governed by sluggish OH^- conduction and oxygen-reduction-reaction kinetics in the cathode due to water deficiency at high current density. Changing the membrane properties and thickness to decrease its water-transport resistance can alleviate some of the water-management concerns. Cathode dehydration is better alleviated with the increase in membrane water diffusivity compared to the decrease in membrane thickness. Asymmetric humidification as a strategy to optimize water management, where increasing the cathode inlet relative humidity does not necessarily improve performance because the correlation of performance with external humidification is determined by the difference in water-transport resistance between anode and cathode toward reaching the cathode catalyst layer where it is consumed. The anode inlet relative humidity is more critical if the membrane has a low water-transport resistance. It is expected that as AEMFC cell development proceeds and performance increases, the examined water-management aspects will only become more critical. Finally, it was shown that high-current-density operation can reduce CO_2-derived bicarbonate content in the membrane-electrode-assembly through CO_2 self-purge at the anode. Performance with 400 ppm CO_2 in the cathode stream could be comparable to that of CO_2-free air at high current densities although not at lower current densities. Overall, AEMFCs demonstrate a much more complex and sensitive water balance compared to those of PEMFCs, and mathematically modeling is ideally suited to understand and optimize the associated tradeoffs.

Acknowledgment

The work was funded by the Fuel Cell Technologies Office (FCTO), Office of Energy Efficiency and Renewable Energy (EERE), of the U. S. Department of Energy under contract number DE-AC02-05CH11231. We thank Bryan Pivovar and KC Neyerlin for helpful discussions.

Downloaded on 2018-02-06 to IP 131.243.172.153 address. Redistribution subject to ECS terms of use (see ecsdl.org/site/terms_use) unless CC License in place (see abstract).

List of Symbols

a_0	Activity of water in membrane
C_t	Fixed charge concentration, mol/L
D_α	Membrane water diffusion coefficient in phase α, m^2/s
F	Faraday constant, 96485 C/mol
i	Volumetric current density, A/m^3
p_i	Partial pressure of gas species i, Pa
R	Ideal-gas constant, J/mol/K
R_k	Resistance on side k, s/cm
S	Membrane liquid-saturated fraction
T	Temperature, K
U_i	Equilibrium potential of electrode reaction i, V
$\overline{V}_M$	Molar volume of membrane, m^3/mol
$\overline{V}_w$	Molar volume of liquid water, m^3/mol
y_i	Mole fraction of ionic species i

Greek

α	Phase, transfer coefficient or vapor/liquid-equilibrated transport coefficient
β	Normalized membrane water flux
ε_M	Ionomer volume fraction
η_i	Overpotential of electrode reaction i, V
κ_α	Membrane ionic conductivity in phase α, S/m
λ	Membrane water content
ξ	Electro-osmotic coefficient
Φ	Potential, V

References

1. T. Burchardt, P. Gouerec, E. Sanchez-Cortezon, Z. Karichev, and J. H. Miners, *Fuel*, **81**, 2151 (2002).
2. X. M. Ge, A. Sumboja, D. Wuu, T. An, B. Li, F. W. T. Goh, T. S. A. Hor, Y. Zong, and Z. L. Liu, *Acs Catalysis*, **5**, 4643 (2015).
3. W. Yang, T. P. Fellinger, and M. Antonietti, *Journal of the American Chemical Society*, **133**, 206 (2011).
4. M. A. Kostowskyj, R. J. Gilliam, D. W. Kirk, and S. J. Thorpe, *International Journal of Hydrogen Energy*, **33**, 5773 (2008).
5. W. C. Sheng, H. A. Gasteiger, and Y. Shao-Horn, *Journal of the Electrochemical Society*, **157**, B1529 (2010).
6. M. T. M. Koper, *Nature Chemistry*, **5**, 255 (2013).
7. P. J. Rheinlander, J. Herranz, J. Durst, and H. A. Gasteiger, *Journal of the Electrochemical Society*, **161**, F1448 (2014).
8. Y. Wang, G. W. Wang, G. W. Li, B. Huang, J. Pan, Q. Liu, J. J. Han, L. Xiao, J. T. Lu, and L. Zhuang, *Energy & Environmental Science*, **8**, 177 (2015).
9. S. Huo, H. Deng, Y. F. Chang, and K. Jiao, *International Journal of Hydrogen Energy*, **37**, 18389 (2012).
10. S. Rowshanzamir, M. Kazemeini, and M. K. Isfahani, *International Journal of Hydrogen Energy*, **23**, 499 (1998).
11. H. Zhang, H. Ohashi, T. Tamaki, and T. Yamaguchi, *Journal of Physical Chemistry C*, **116**, 7650 (2012).
12. H. Zhang, H. Ohashi, T. Tamaki, and T. Yamaguchi, *Journal of Physical Chemistry C*, **117**, 16791 (2013).
13. J. R. Varcoe, P. Atanassov, D. R. Dekel, A. M. Herring, M. A. Hickner, P. A. Kohl, A. R. Kucernak, W. E. Mustain, K. Nijmeijer, K. Scott, T. W. Xu, and L. Zhuang, *Energy & Environmental Science*, **7**, 3135 (2014).
14. L. A. Adams, S. D. Poynton, C. Tamain, R. C. T. Slade, and J. R. Varcoe, *Chemsuschem*, **1**, 79 (2008).
15. A. M. Kiss, T. D. Myles, K. N. Grew, A. A. Peracchio, G. J. Nelson, and W. K. S. Chiu, *Journal of the Electrochemical Society*, **160**, F994 (2013).
16. O. I. Deavin, S. Murphy, A. L. Ong, S. D. Poynton, R. Zeng, H. Herman, and J. R. Varcoe, *Energy & Environmental Science*, **5**, 8584 (2012).
17. M. C. Kimble and R. E. White, *Journal of the Electrochemical Society*, **138**, 3370 (1991).
18. M. Duerr, S. Gair, A. Cruden, and J. McDonald, *Journal of Power Sources*, **171**, 1023 (2007).
19. I. Verhaert, M. De Paepe, and G. Mulder, *Journal of Power Sources*, **193**, 233 (2009).
20. I. Verhaert, S. Verhelst, G. Janssen, G. Mulder, and M. De Paepe, *International Journal of Hydrogen Energy*, **36**, 11011 (2011).
21. K. Jiao, P. He, Q. Du, and Y. Yin, *International Journal of Hydrogen Energy*, **39**, 5981 (2014).
22. H. Deng, D. W. Wang, X. Xie, Y. B. Zhou, Y. Yin, Q. Du, and K. Jiao, *Renewable Energy*, **91**, 166 (2016).
23. I. Kruusenberg, L. Matisen, Q. Shah, A. M. Kannan, and K. Tammeveski, *International Journal of Hydrogen Energy*, **37**, 4406 (2012).
24. T. J. Omasta, L. Wang, X. Peng, C. A. Lewis, J. R. Varcoe, and W. E. Mustain, *Journal of Power Sources*, (2017).
25. A. Z. Weber and J. Newman, *Journal of the Electrochemical Society*, **151**, A311 (2004).
26. Y. S. Li, T. S. Zhao, and W. W. Yang, *International Journal of Hydrogen Energy*, **35**, 5656 (2010).
27. A. Kusoglu and A. Z. Weber, *Chem Rev*, **117**, 987 (2017).
28. X. Y. Luo and S. Holdcroft, *J Membrane Sci*, **520**, 155 (2016).
29. J. L. Qiao, L. Xu, L. Ding, P. H. Shi, L. Zhang, R. Baker, and J. J. Zhang, *Int. J. Electrochem. Sci.*, **8**, 1189 (2013).
30. C. C. L. McCrory, S. Jung, I. M. Ferrer, S. M. Chatman, J. C. Peters, and T. F. Jaramillo, *Journal of the American Chemical Society*, **137**, 4347 (2015).
31. Z. B. Zhuang, S. A. Giles, J. Zheng, G. R. Jenness, S. Caratzoulas, D. G. Vlachos, and Y. S. Yan, *Nat Commun*, **7** (2016).
32. K. G. Schulz, U. Riebesell, B. Rost, S. Thoms, and R. E. Zeebe, *Marine Chemistry*, **100**, 53 (2006).
33. I. V. Zenyuk, A. Lamibrac, J. Eller, D. Y. Parkinson, F. Marone, F. N. Buchi, and A. Z. Weber, *Journal of Physical Chemistry C*, **120**, 28701 (2016).
34. Q. J. Duan, S. H. Ge, and C. Y. Wang, *Journal of Power Sources*, **243**, 773 (2013).
35. I. V. Zenyuk, P. K. Das, and A. Z. Weber, *Journal of the Electrochemical Society*, **163**, F691 (2016).
36. H. A. Miller, F. Vizza, M. Marelli, A. Zadick, L. Dubau, M. Chatenet, S. Geiger, S. Cherevko, H. Doan, R. K. Pavlicek, S. Mukerjee, and D. R. Dekel, *Nano Energy*, **33**, 293 (2017).
37. A. Z. Weber, R. L. Borup, R. M. Darling, P. K. Das, T. J. Dursch, W. B. Gu, D. Harvey, A. Kusoglu, S. Litster, M. M. Mench, R. Mukundan, J. P. Owejan, J. G. Pharoah, M. Secanell, and I. V. Zenyuk, *Journal of the Electrochemical Society*, **161**, F1254 (2014).
38. J. Newman and K. E. Thomas-Alyea, *Electrochemical Systems*, John Wiley & Sons, New York (2004).
39. A. Z. Weber and J. Newman, *Journal of the Electrochemical Society*, **151**, A326 (2004).
40. G. J. M. Janssen and M. L. J. Overvelde, *Journal of Power Sources*, **101**, 117 (2001).
41. M. Adachi, T. Navessin, Z. Xie, F. H. Li, S. Tanaka, and S. Holdcroft, *J Membrane Sci*, **364**, 183 (2010).
42. B. Kientiz, H. Yamada, N. Nonoyama, and A. Z. Weber, *Journal of Fuel Cell Science and Technology*, **8**, 011013 (2011).
43. T. P. Pandey, A. M. Maes, H. N. Sarode, B. D. Peters, S. Lavina, K. Vezzu, Y. Yang, S. D. Poynton, J. R. Varcoe, S. Seifert, M. W. Liberatore, V. Di Notob, and A. M. Herring, *Phys Chem Chem Phys*, **17**, 4367 (2015).
44. M. A. Hickner, A. M. Herring, and E. B. Coughlin, *J Polym Sci Pol Phys*, **51**, 1727 (2013).
45. W. A. Rigdon, T. J. Omasta, C. Lewis, M. A. Hickner, J. R. Varcoe, J. N. Renner, K. E. Ayers, and W. E. Mustain, *Journal of Electrochemical Energy Conversion and Storage*, (2017).

Downloaded on 2018-02-06 to IP 131.243.172.153 address. Redistribution subject to ECS terms of use (see ecsdl.org/site/terms_use) unless CC License in place (see abstract).